Powder Technology 477 (2026) 122468

Contents lists available at ScienceDirect

Powder Technology

journal homepage: www.journals.elsevier.com/powder-technology

Three-dimensional CFD-DEM simulations of vibrated fluidized beds validated by real-time MRI: Implications of slice-based versus full-domain analysis

Nick Hildebrandt [a,*], Melis Özdemir [b], Swantje Pietsch-Braune [a], Stefan Benders [b], Alexander Penn [b], Stefan Heinrich [a]

[a] Institute of Solids Process Engineering and Particle Technology, Hamburg University of Technology, Denickestraße 15, Hamburg 21073, Germany
[b] Institute of Process Imaging, Hamburg University of Technology, Denickestraße 17, Hamburg 21073, Germany

HIGHLIGHTS

- Comparison of MRI data to CFD-DEM of vibrated and non-vibrated fluidized beds.
- CFD-DEM reproduces MRI trends in bubble and bed parameters.
- CFD-DEM slightly overpredicts bubble size and bed height, underpredicts bubble count.
- No systematic vibration effect observed for vibration acceleration $\Gamma < 1$ at 2–4 U_{mf}.
- Slice analysis captures trends but differs systematically from full 3D evaluation.

GRAPHICAL ABSTRACT

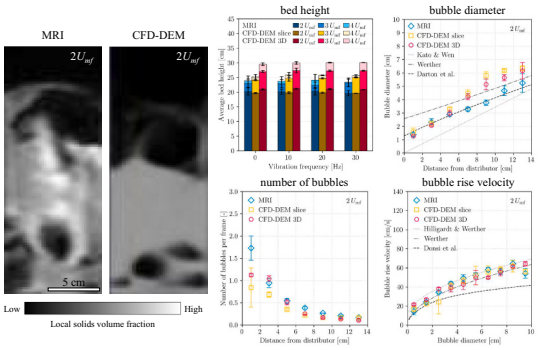

ARTICLE INFO

Keywords:
Fluidization
Vibrated fluidized bed
CFD-DEM
MRI
Bubble properties

ABSTRACT

This study compares real-time magnetic resonance imaging (MRI) measurements with three-dimensional CFD-DEM simulations for fluidized beds of Geldart Group D particles under non-vibrated and vibrated conditions. Simulation data were analyzed both in a central 10 mm slice, mimicking the MRI measurement, and across the full three-dimensional domain to assess the representativeness of slice-based evaluation. Bed height, bubble diameter, bubble count, and bubble rise velocity were quantitatively compared. For non-vibrated cases, CFD-DEM agrees well with MRI across all metrics and reproduces established correlations for bubble diameter and rise velocity. For vibrated conditions at 10–30 Hz and 0.5 mm peak-to-peak amplitude (dimensionless acceleration $\Gamma < 1$) and superficial gas velocities of 2–4 U_{mf}, no systematic changes in bed expansion or bubble-scale properties was observed. These findings indicate that, for Geldart D particles operating well above minimum fluidization, gas-driven bubbling dominates bed hydrodynamics and low-to-moderate vibration intensities do not substantially alter macroscopic behavior. Comparing slice-based and full-domain analyses revealed systematic offsets in absolute values, most notably in bed height and small-bubble statistics. Thus, central-slice measurements capture hydrodynamic trends reliably but can bias absolute quantities relative to full three-dimensional

* Corresponding author.
E-mail address: nick.hildebrandt@tuhh.de (N. Hildebrandt).

https://doi.org/10.1016/j.powtec.2026.122468
Received 14 November 2025; Received in revised form 13 February 2026; Accepted 22 March 2026
Available online 24 March 2026

evaluation. These results define a regime of weak vibration influence for Geldart D particles and provide guidance for interpreting tomographic measurements of fluidized beds.

Notation

A	vibration amplitude (m)
C_d	drag coefficient
CFL	Courant number
d_{32}	Sauter diameter (m)
d_p	particle diameter (m)
$e_{p\text{-}p}$	restitution coefficient particle/particle
$e_{p\text{-}w}$	restitution coefficient particle/wall
f	vibration frequency (Hz)
$F_{c,i}$	contact force (N)
$F_{d,i}$	drag force (N)
$F_{fp,i}$	fluid-particle interaction forces (N)
Fr	Froude number
g	gravitational acceleration (m/s^2)
I_i	inertia tensor (kg•m^2)
m_i	mass of component i (kg)
M_i	torque (Nm)
N_p	number of particles
p	static pressure (Pa)
p_{outlet}	outlet pressure (Pa)
R	radius of rotating drum (m)
R_{fp}	momentum exchange term (N/m^3)
$Re_{p,i}$	Reynolds number of particles
t	time (s)
Δt_{CFD}	CFD time step (s)
Δt_{DEM}	DEM time step (s)
U_f	fluid velocity (m/s)
$U_{f,in}$	superficial gas inlet velocity (m/s)
U_{mf}	minimum fluidization velocity (m/s)
$U_{p,i}$	particle velocity (m/s)
V_{cell}	volume of a CFD grid cell (m^3)
$V_{p,i}$	particle volume (m^3)
x_i	center of mass of component i (m)
Δx	size of a grid cell (m)
Y_p	Young's modulus of the particles (Pa)
Y_w	Young's modulus of the wall (Pa)

Greek letters

α_f	fluid volume fraction
β_i	momentum exchange coefficient (kg/(m^3•s))
Γ	vibration intensity
μ_f	fluid dynamic viscosity (kg/(m•s))
$\mu_{r,p\text{-}p}$	rolling friction coefficient particle/particle
$\mu_{r,p\text{-}w}$	rolling friction coefficient particle/wall
$\mu_{s,p\text{-}p}$	static friction coefficient particle/particle
$\mu_{s,p\text{-}w}$	static friction coefficient particle/wall
ν_f	Fluid kinematic viscosity (m^2/s)
ν_p	Poisson ratio of the particles
ν_w	Poisson ratio of the wall
ρ_f	fluid density (kg/m^3)
ρ_p	particle density (kg/m^3)
τ_f	stress tensor for the fluid phase (Pa)
ω	angular velocity (rad/s)

Abbreviations

CFD	computational fluid dynamics
DEM	discrete element method
MRI	magnetic resonance imaging
PISO	pressure-implicit with splitting of operators
VFB	vibrating fluidized bed

1. Introduction

Fluidized beds are widely utilized in various industries due to their excellent gas-solid contact and efficient solid mixing capabilities. Mechanical vibration is often added to improve fluidization behavior. In vibrating fluidized beds (VFBs), vibratory kinetic energy is introduced through oscillatory displacement of the bed vessel. This mechanical vibration effectively reduces minimum fluidization velocity [1–3] and improves particle mixing and contact efficiency [4,5]. VFBs are particularly effective for processing cohesive particles, where the additional energy can minimize agglomeration and prevent gas channeling [6,7]. Introducing vibration significantly increases system complexity, making experimental characterization and modeling more challenging. The interaction between vibration and bubble dynamics in the bubbling regime further complicates the system behavior, underscoring the critical need for comprehensive experimental and computational characterization of vibrating fluidized bed systems.

Traditionally, the investigation of fluidized bed hydrodynamics has relied primarily on intrusive probes and optical measurements of pseudo-2D fluidized beds. Intrusive probes, such as pressure sensors and capacitance probes, provide only single-point measurements and may interfere with natural flow patterns. Pseudo-2D configurations, on the other hand, are strongly influenced by wall effects, which can limit their representativeness of three-dimensional fluidized bed behavior [8,9]. Although wall effects are also present in laboratory-scale cylindrical fluidized beds, such systems allow three-dimensional flow development and more representative bubble dynamics. To overcome the limitations of traditional measurement methods, tomographic techniques are increasingly employed for fluidized bed characterization. These non-invasive methods include X-ray computed tomography [10], electrical capacitance (volume) tomography [11,12], positron emission particle tracking [13], and magnetic resonance imaging (MRI). A historical limitation of MRI has been its relatively low temporal resolution, which restricted measurements to time-averaged data with acquisition times on the order of minutes [14]. Recent advances in scan acceleration techniques, including optimized radiofrequency detector design and improved scan sequence efficiency, have dramatically enhanced temporal resolution, enabling real-time MRI of fluidized beds [15]. This breakthrough allows the capture of instantaneous gas bubble positions and particle velocities, making MRI particularly well suited for obtaining spatially and temporally resolved dynamic information from the interior of fluidized beds. Real-time MRI has been applied in fluidized bed research to investigate bubble behavior and particle velocities [16], quantify the effects of liquid bridging on fluidization hydrodynamics [17], study single isolated bubbles injected into incipiently fluidized beds [18], and assess the influence of different baffles and internals on gas-solid fluidized bed hydrodynamics [19–21]. Real-time MRI measurements are typically based on data acquired from limited slice thicknesses, and it therefore remains unclear to what extent such slice-based observations are representative of bubble dynamics and bed hydrodynamics throughout the full three-dimensional fluidized bed. While

tomographic techniques have significantly advanced fluidized bed research, their application to VFBs remains limited, with most experimental studies relying on pseudo-2D configurations [22–26].

Complementing experimental investigations, computational fluid dynamics coupled with discrete element method (CFD-DEM) simulations have emerged as a powerful tool for studying fluidized bed hydrodynamics. In this approach, the gas phase is treated as a continuum using computational fluid dynamics, while individual particles are modeled using the discrete element method, enabling detailed analysis of gas-particle interactions and particle-scale phenomena. This coupled modeling framework has proven particularly valuable for investigating complex multiphase systems where experimental measurements alone may be insufficient to capture all relevant physics. CFD-DEM simulations have successfully reproduced key hydrodynamic features of conventional fluidized beds, including bubble formation, particle mixing patterns, and pressure drop characteristics [27–29]. Several studies have extended CFD-DEM to VFBs, focusing primarily on the influence of vibration frequency and amplitude on bed dynamics [23,26,30–35]. Similar to experimental investigations, these CFD-DEM studies have largely been restricted to pseudo-2D [23,26,30–33] or strictly two-dimensional [34,35] computational domains. Such simplifications are primarily adopted to reduce computational cost and complexity, as fully three-dimensional simulations require substantially higher computational resources due to the large number of particles involved. In addition, suitable experimental data for three-dimensional VFBs are scarce. As a consequence, quantitative experimental validation of three-dimensional CFD-DEM simulations of VFBs remains limited, and the accuracy of such models in predicting bubble-scale hydrodynamics in realistic three-dimensional systems remains largely unassessed. In addition, it remains largely unexplored how results obtained from full three-dimensional CFD-DEM simulations should be analyzed and compared to slice-based experimental measurements.

The primary objective of this work is to validate three-dimensional CFD-DEM simulations against real-time MRI measurements for fluidized beds of Geldart Group D particles under both non-vibrated and vibrated conditions. MRI is employed as a non-invasive experimental benchmark providing time-resolved, bubble-scale information, while CFD-DEM is treated as the numerical model under validation. The comparison focuses on key bubble properties and bed hydrodynamic parameters, including bed height, bubble diameter, bubble count, and bubble rise velocity, across different superficial gas velocities and vibration conditions. In addition, two analysis approaches are applied to the CFD-DEM data – a slice-based method mimicking the MRI measurements and a full three-dimensional analysis – to assess how experimental measurement limitations affect the interpretation of fluidized-bed hydrodynamics. Within this validation framework, the influence of mechanical vibration is examined.

2. MRI measurements

2.1. Experimental setup

Experiments were conducted in an MRI-compatible fluidized bed constructed from polymethyl methacrylate (PMMA) with an outer diameter of 100 mm and an inner diameter of 96 mm. The bed was open to the atmosphere with a filter covering the top to prevent particle elutriation. Pressurized air served as the fluidizing medium, with volumetric flow rates controlled via a mass flow controller (F-202AV, Bronkhorst) to achieve superficial gas velocities of 2, 3, and 4 U_{mf}. Minimum fluidization velocity U_{mf} was determined experimentally to be 0.30 m/s by monitoring pressure drop across the bed at progressively decreasing gas velocities. Uniform gas distribution was achieved through a sintered porous polyethylene plate with 20 μm pore size and 5 mm thickness located at the bottom of the bed. The fluidized bed was filled with poppy seeds to a static bed height of 116 mm. The particle size distribution of the poppy seeds was measured by dynamic image analysis using a Camsizer XT (Microtrac Retsch GmbH) and is shown in Fig. 1. The detected particle areas were converted to equivalent spherical diameters, yielding a median diameter of 1.05 mm and a Sauter diameter of 1.17 mm. The particle density of 1165 kg/m^3 was measured using a helium gas pycnometer (AccuPyc 1330, Micromeritics). According to these properties, the material is classified as Geldart Group D.

Mechanical vibration was applied using an electrodynamic shaker (M120-CE, IMV Corporation). Since the isocenter of the magnet is located approximately 4 m above ground level, glass-fiber reinforced tubes were used to transmit the vibrations from the shaker to the elevated bed assembly. Vibration frequencies of 10, 20, and 30 Hz at a fixed peak-to-peak amplitude of 0.5 mm were used to generate sinusoidal vertical oscillations of the entire bed assembly. The vibration frequencies and amplitude were selected to (i) match the mechanically stable operating range of the experimental setup and (ii) span vibration intensities commonly reported in laboratory-scale vibrating fluidized-beds. The corresponding dimensionless acceleration

$$\Gamma = \frac{(2\pi f)2A}{g}, \tag{1}$$

covers approximately 0.1–0.9, representing a low-to-moderate vibration intensity range within the scope of laboratory-scale studies.

MRI measurements were performed using a vertical 3 Tesla MRI system equipped with a custom-built 15-channel RF detector array for signal detection. The natural oil content within poppy seeds provided the MRI-active signal source, allowing gas bubbles to be distinguished through the signal-intensity voids created in the acquired images. The use of the multichannel detector array enabled parallel imaging, wherein the spatial sensitivity of each coil element is exploited to reconstruct the full image [36]. This technique substantially reduced the required sampling density, thereby achieving enhanced temporal resolution necessary for capturing transient bubble dynamics. Images were acquired with a temporal resolution of 18 ms and an in-plane resolution of 4 mm × 8 mm. The imaging field-of-view encompassed the complete expanded bed region. Signal intensities from a central 10 mm-thick vertical slice through the bed centerline were spatially averaged, yielding two-dimensional projections. At each operating condition, 500 consecutive frames were recorded using a gradient echo pulse sequence, corresponding to a total sampling duration of approximately 9 s. Considering the observed bubble rise velocities and bed heights, this duration includes a large number of independent bubble formation and eruption events across all investigated gas velocities.

Table 1 summarizes the varied operating parameters and their respective values. All combinations of superficial gas velocity and vibration frequency were investigated. Each combination was repeated three times. Mean values and standard deviations were calculated from

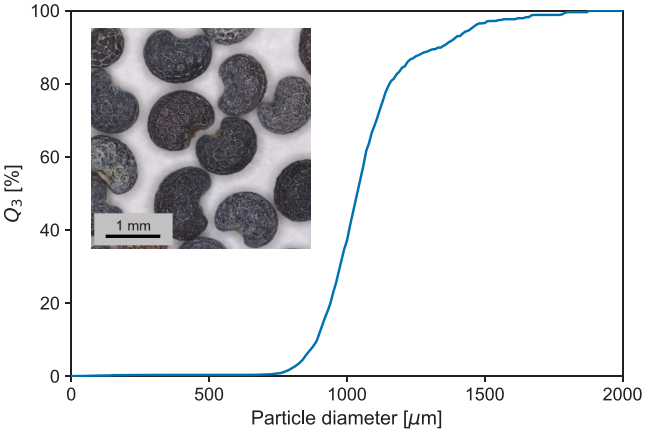

Fig. 1. Volume-based particle size distribution and light microscope image of poppy seeds.

Table 1
Parameters varied during experiments.

Property	Symbol	Values			Unit
Superficial gas inlet velocity	$U_{f,in}$	2 U_{mf}	3 U_{mf}	4 U_{mf}	m/s
Vibration frequency	f	10	20	30	Hz

the three repetitions, with standard deviations shown as error bars in the results figures.

2.2. Post-processing of MRI data

Acquired MRI images were processed using Python with the OpenCV library to segment and quantify gas bubbles within the fluidized bed. Threshold-based segmentation was used to differentiate low signal intensity gas bubbles from high signal intensity particle regions. Morphological operations such as dilation and erosion were used to reduce noise and smooth bubble edges.

Area-equivalent bubble diameters were calculated from the segmented bubble regions assuming circular geometry. Bubble dynamics were quantified by tracking bubble centroids across consecutive frames separated by the 18 ms temporal resolution. Tracking was based on direct pixel overlap between segmented regions in successive frames, enabling classification of bubble events into tracks (1-to-1 continuation), splits (1-to-n), and merges (n-to-1). Only unambiguous 1-to-1 continuation events persisting over at least three consecutive frames were considered as accepted tracks. Bubble events involving splitting (1-to-n) or merging (n-to-1) were excluded from velocity calculations, as these events do not allow for a unique definition of bubble displacement. Instantaneous bubble rise velocities were then calculated for accepted tracks based on the centroid displacement over the time interval. Furthermore, the fluidized bed height was determined by tracking the highest particle-containing pixel row in each frame and averaging the result.

The spatial resolution of the MRI measurements imposes a lower limit on the size of gas structures that can be reliably detected. Small bubbles, particularly in the vicinity of the distributor where gas injection occurs, may therefore not be fully resolved or may be filtered out during threshold-based segmentation. In addition, the choice of signal intensity threshold can influence bubble boundaries and thus affect absolute bubble size and count statistics. However, the same post-processing procedure and thresholding criteria were consistently applied across all operating conditions, ensuring that relative comparisons between cases remain meaningful.

3. Numerical simulations

For the simulations in this work, the open source CFD code OpenFOAM [37] and the DEM code LIGGGHTS [38] were coupled using CFDEMcoupling [39]. Since close to 900,000 particles were simulated, the unresolved coupling method was required. In unresolved simulations, the computational grid cell size exceeds the particle diameter, as particles are not fully resolved within the CFD simulation. Instead, their presence is accounted for through momentum exchange terms and void fraction calculations. As a solver for coupling granular flow with fluid flow, *cfdemSolverPiso* was used, which applies a PISO (Pressure-Implicit with Splitting of Operators) loop for pressure velocity coupling. PISO was selected because the simulations are fully transient and incompressible, with time steps constrained by the CFL condition and DEM coupling, for which PISO provides stable and efficient pressure-velocity coupling. Further details about the CFD-DEM coupling routine can be found in the publication of Goniva et al. [39].

3.1. Gas phase

The gas phase was assumed to be incompressible, which is justified due to the constant temperature and low Mach number throughout the whole system. Under this assumption, the dynamics of the fluid phase in the presence of a particulate phase can be described by the Navier-Stokes equations expressed as:

$$\frac{\partial}{\partial t}\alpha_f + \nabla \bullet \left(\alpha_f U_f\right) = 0, \tag{2}$$

$$\frac{\partial}{\partial t}\left(\rho_f \alpha_f U_f\right) + \nabla \bullet \left(\rho_f \alpha_f U_f U_f\right) = -\alpha_f \nabla p + \nabla \bullet \left(\alpha_f \tau_f\right) - R_{fp}. \tag{3}$$

Here α_f is the fluid volume fraction, U_f the fluid velocity, ρ_f the fluid density, p the static pressure, τ_f the stress tensor for the fluid phase, and R_{fp} the momentum exchange term. For calculating the fluid volume fraction α_f, each particle is decomposed into a cloud of 29 distributed marker points, allowing the particle's volume to be proportionally allocated across all computational cells it partially occupies. For incompressible flows with constant viscosity, the stress term $\nabla \bullet \left(\alpha_f \tau_f\right)$ can be expressed as $\mu_f \nabla^2\left(\alpha_f U_f\right)$, where μ_f is the dynamic viscosity of the fluid. The momentum exchange term R_{fp} includes each particle's contribution to particle-fluid momentum exchange within a computational cell of volume V_{cell} and can be expressed as a drag force sum:

$$R_{fp} = \frac{1}{V_{cell}} \sum_i F_{d,i}, \tag{4}$$

where

$$F_{d,i} = \beta_i V_{p,i}\left(U_f - U_{p,i}\right). \tag{5}$$

$V_{p,i}$ and $U_{p,i}$ are the volume and velocity of particle i, respectively. The momentum exchange coefficient β_i is calculated based on drag correlations. Here the drag model by Gidaspow [40], which is a combination of the Ergun Eq. [41] and the Wen and Yu Eq. [42], was used. The Gidaspow drag model switches between the two correlations depending on the fluid volume fraction. For fluid volume fractions $\alpha_f > 0.8$, the Wen and Yu correlation applies:

$$\beta_i = \frac{3}{4} C_d \frac{\alpha_f\left(1-\alpha_f\right)\left|U_f - U_{p,i}\right|\rho_f}{d_{p,i}} \alpha_f^{-2.65}, \tag{6}$$

with

$$C_d = \frac{24}{\alpha_f Re_{p,i}}\left[1 + 0.15\left(\alpha_f Re_{p,i}\right)^{0.687}\right], \tag{7}$$

$$Re_{p,i} = \frac{\left|U_f - U_{p,i}\right| d_{p,i}}{\nu_f}, \tag{8}$$

where $d_{p,i}$ is the particle diameter and ν_f is the kinematic viscosity of the fluid. For fluid volume fractions $\alpha_f \leq 0.8$, the Ergun equation is used:

$$\beta_i = 150 \frac{\left(1-\alpha_f\right)^2 \nu_f \rho_f}{\alpha_f {d_{p,i}}^2} + 1.75 \frac{\left(1-\alpha_f\right)\left|U_f - U_{p,i}\right|\rho_f}{d_{p,i}}. \tag{9}$$

The Gidaspow drag model was selected due to its ability to represent both dense and dilute regimes encountered in fluidized beds. The model employs a sharp transition between the Ergun and Wen-Yu correlations, which may influence the predicted interphase momentum exchange in regions of intermediate solids concentration and strong voidage gradients.

3.2. Solid phase

In the DEM approach, as initially proposed by Cundall and Strack [43], the trajectories of individual particles i of mass m_i are calculated by applying the Newtonian laws of motion:

$$m_i \frac{d^2}{dt} x_i = F_{c,i} + F_{fp,i} + m_i g, \tag{10}$$

$$I_i \frac{d}{dt}\omega_i = \sum_i M_i, \tag{11}$$

with center of mass positions x_i, sum of all contact forces $F_{c,i}$, sum of all fluid-particle interaction forces acting on the particle $F_{fp,i}$, gravitational vector g, inertia tensors I_i, angular velocities ω_i, and torques M_i. For modeling particle interactions, the soft-sphere approach [43] was used where normal contact forces are calculated according to the Hertz-Mindlin law, utilizing a non-linear spring-dashpot model [44]. Similarly, tangential contact forces were calculated via a non-linear spring-dashpot model with an upper bound established by the Coulomb friction criterion [44]. Rolling friction was modeled using an elastic-plastic spring-dashpot model as detailed in the publication of Ai et al. [45]. The fluid-particle interaction forces $F_{fp,i}$ included three components: forces arising from viscous effects, pressure gradients, and drag. Additional fluid-particle interactions like virtual mass and Basset forces were neglected due to the substantial density ratio between the solid particles and the surrounding gas phase [46].

3.3. Case setup

For the simulations, polydispersity was introduced in the form of a particle size distribution with three discrete classes, to prevent crystallization effects of the packing, that can occur in monodisperse particle arrangements [47]. The particle size distribution was centered on a target diameter of 1.05 mm, with two additional classes positioned at ±15% of this value. The weights of each class were adjusted to produce a Sauter diameter d_{32} of 1.17 mm. The particles were assumed to be perfect spheres, even though their sphericity was measured to only be 0.87.

These idealizations of particle size distribution and particle shape may influence particle-scale contact mechanics and gas-particle interactions. To account for these effects at the bulk scale relevant to fluidized-bed hydrodynamics, DEM model parameters were calibrated by matching simulated bulk behavior to experimentally measured static and dynamic angles of repose, bulk friction angle, bulk cohesion, and bulk density [48,49]. While this calibration approach is effective in reproducing macroscopic bulk properties, it cannot fully capture all particle-scale effects associated with non-sphericity and size variability. A systematic optimization approach based on Latin Hypercube Sampling and Kriging was employed to identify suitable DEM parameters. A detailed description of the calibration experiments and optimization procedure is provided in the Supplementary Information. The resulting calibrated DEM parameters used in the simulations are summarized in Table 2.

Table 2
DEM model parameters used in simulations.

Parameter	Symbol	Value	Unit
Particle diameter	d_p	1.05	mm
Particle density	ρ_p	1015	kg/m^3
Number of particles	N_p	894,394	–
Young's modulus			
Particles	Y_p	1e7	Pa
Wall	Y_w	1e7	Pa
Poisson ratio			
Particles	ν_p	0.3	–
Wall	ν_w	0.3	–
Restitution coefficient			
Particle-particle	$e_{p\text{-}p}$	0.90	–
Particle-wall	$e_{p\text{-}w}$	0.77	–
Coefficient of static friction			
Particle-particle	$\mu_{s,p\text{-}p}$	0.13	–
Particle-wall	$\mu_{s,p\text{-}w}$	0.87	–
Coefficient of rolling friction			
Particle-particle	$\mu_{r,p\text{-}p}$	0.84	–
Particle-wall	$\mu_{r,p\text{-}w}$	0.58	–

Fig. 2 shows the CFD grid that was used for the simulations. The grid was generated with blockMesh, a mesher contained in OpenFOAM, and classy_blocks, a utility for the creation of blockMesh dictionaries. The grid cell edge length ranged between 2.6 and 5.4 mm with the average edge length being 3.2 mm. Across all three particle sizes, this gives grid-size-to-particle-diameter ratios of 2.2–6.1 with an average ratio of 3.15. Thus, the grid size is close to the suggested values in the literature to obtain mesh-independent solutions [47,48].

The inlet area at the bottom was defined as constant superficial gas velocity inlet, while the outlet at the top was set to be a pressure outlet with a gauge pressure of zero. The wall boundary condition was set to no-slip for the gas phase and rigid wall for the particles. The density and kinematic viscosity of the gas were set to 1.2 kg/m^3 and 1.5•10^{-5} m^2/s, respectively, which corresponds to air at atmospheric pressure and 20 °C. The CFL condition $CFL = max\frac{U_f \Delta t_{CFD}}{\Delta x} < 1$, where Δx is the size of a grid cell, was used to choose the CFD time step Δt_{CFD}. The DEM time step Δt_{DEM} was set to approximately 10% of the Rayleigh time based on the calibrated model parameters. The simulations were run for 15 s of simulation time, of which the last 10 s were used for the analysis. Similar to the procedure for the experimental part, the minimum fluidization velocity was determined by simulating defluidization. The simulated minimum fluidization velocity was found to be 0.31 m/s, demonstrating good agreement with the experimental value (0.30 m/s). Table 3 gives a summary of the fluid phase properties and simulation conditions.

Vibration was modeled by oscillating the gravitational force. To achieve this, the gravitational acceleration in both CFD and DEM was modified according to $\vec{g} = 9.81 + (2\pi f)^2 A \sin(2\pi f t)$, where f is the vibration frequency, $A = 0.25$ mm corresponds to the applied vibration amplitude (0.5 mm peak-to-peak), and t is the time. Modeling vibration through an oscillating gravitational acceleration is equivalent to solving the governing equations in a non-inertial reference frame moving with the vertically oscillating fluidized bed [31,49]. This formulation effectively accounts for the motion of the distributor and sidewalls without explicitly prescribing boundary motion and avoids the need for a moving mesh. While this approach applies a spatially uniform acceleration and therefore does not explicitly resolve possible time delays or dissipative effects associated with the transmission of vibration-induced stresses from the walls into the bed, it provides a physically consistent representation of vibration-induced inertial forcing and is widely used to study global hydrodynamics in vibrated fluidized beds [26,30–32,49,50].

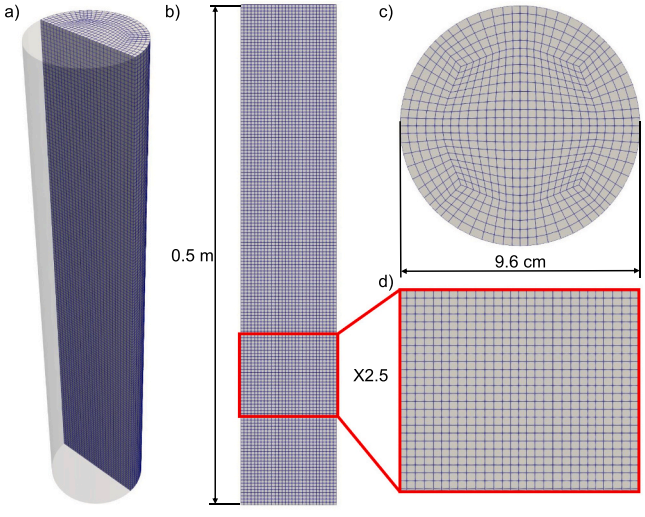

Fig. 2. CFD grid. (a) 3D view; (b) Axial cross-section; (c) Radial cross-section; and (d) × 2.5 magnified view of axial cross-section showing the grid structure.

Table 3
Fluid phase properties and simulation conditions.

Property	Symbol	Value	Unit
Fluid phase density	ρ_f	1.2	kg/m^3
Fluid kinematic viscosity	ν_f	$1.5 \bullet 10^{-5}$	m^2/s
Outlet pressure	p_{outlet}	0	Pa
Time step			
CFD	Δt_{CFD}	$2.5 \bullet 10^{-4}$	s
DEM	Δt_{DEM}	$2.5 \bullet 10^{-6}$	s

3.4. Post-processing of simulation data

To ensure a direct comparison between experimental and simulation results, the post-processing of the simulation data matches the MRI data processing as closely as possible. Therefore, the central slice of the simulated void fraction field was extracted and averaged to create two-dimensional images matching the MRI data format. The same bubble detection and characterization algorithms used for MRI data processing were applied to these simulation-generated images. In addition to this slice-based approach, the full three-dimensional void fraction field was analyzed to assess whether the central slice results are representative of the entire fluidized bed system and to capture bubble behavior that may

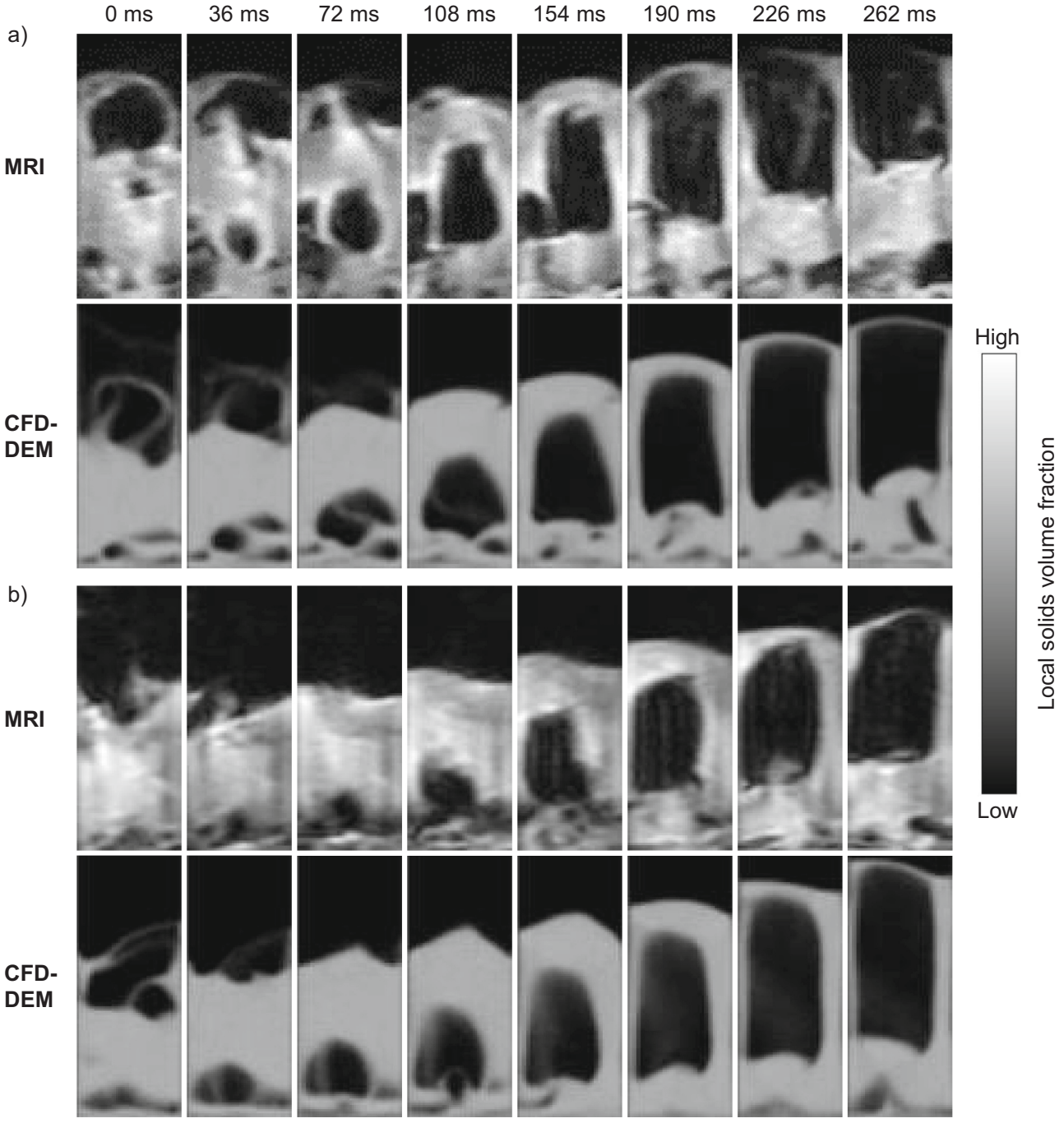

Fig. 3. Time series of instantaneous snapshots of the local solids volume fraction in the central 10 mm slice obtained from MRI measurements (top rows) and CFD-DEM simulations (bottom rows) at superficial gas velocity $U_{f,in} = 2\ U_{mf}$ for a) a non-vibrated fluidized bed and b) a vibrated fluidized bed ($f = 30$ Hz, $A = 0.5$ mm peak-to-peak).

not be detected within the limited spatial region of the slice analysis. The 3D method uses algorithms that follow the same principles as the slice method but operate on the complete computational domain. From here on, these approaches are referred to as the CFD-DEM slice method and the CFD-DEM 3D method, respectively. Both methods were processed with the same temporal resolution of 18 ms as the MRI measurements. While the MRI data used signal-intensity thresholds and the CFD-DEM data used void-fraction thresholds, equivalent criteria were applied to identify and segment bubbles. Additional processing parameters, such as minimum bubble area and connectivity criteria, were kept consistent between the two methods to ensure comparable bubble detection and characterization.

4. Results and discussion

4.1. Qualitative comparison

Section 4.1 provides a qualitative comparison of bubble dynamics observed in the MRI measurements and CFD-DEM simulations and establishes a baseline for interpreting the quantitative results presented in the following sections. The focus is on assessing qualitative agreement between the experiment and simulation and identifying the dominant hydrodynamic mechanisms governing bubble formation and rise under non-vibrated and vibrated conditions.

Fig. 3 presents representative time series of instantaneous snapshots of the local solids volume fraction in the central 10 mm slice of the bed at a superficial gas velocity of $U_{f,in} = 2\ U_{mf}$, with snapshots shown at 36 ms intervals. The top rows correspond to MRI measurements, where grayscale intensity reflects signal intensity, while the bottom rows show CFD-DEM simulation results, where grayscale values represent the local solids volume fraction.

For the non-vibrated case (Fig. 3a), the complete life cycle of a bubble can be observed in both MRI and CFD-DEM results. Bubbles nucleate in the lower bed region, grow as they ascend, and ultimately burst at the bed surface. Bubble growth is partially driven by coalescence of smaller bubbles, which is particularly evident between 108 and 190 ms in the MRI time series and between 36 and 108 ms in the corresponding CFD-DEM time series. Overall, both approaches reproduce bubble shape, growth, and rise behavior qualitatively, indicating strong agreement between the experiment and simulation. This agreement is not limited to the selected time series but is consistently observed across longer-duration recordings for all investigated operating conditions.

Representative snapshots from a vibrated case ($f = 20$ Hz, $A = 0.5$ mm peak-to-peak) are shown in Fig. 3b. A direct qualitative comparison with the non-vibrated case reveals similar bubble formation, growth, and rise behavior in both the MRI measurements and the CFD-DEM simulations. Within the investigated vibration amplitude and frequency range, no pronounced qualitative changes in bubble morphology or rise behavior are observed. The observed qualitative similarity between vibrated and non-vibrated cases can be interpreted in the context of the investigated operating regime. The vibration intensity Γ ranges from approximately 0.1–0.9 for the present conditions, indicating that the imposed vibration acceleration remains comparable to or smaller than gravity. In addition, the relative contribution of vibration-induced motion compared to gas-driven motion can be assessed by comparing the characteristic velocities associated with vibration and gas flow. This yields the dimensionless ratio

$$\frac{(2\pi f A)2}{U_{f,in}^2}, \tag{12}$$

which represents the ratio of vibration-related to gas-related kinetic energy per unit mass. For the present operating conditions, this ratio remains in the order of 10^{-4}–10^{-2}, indicating that gas-driven hydrodynamics dominate the bed behavior under the investigated conditions. Previous experimental and numerical studies on vibrated fluidized beds of Geldart Group D particles have demonstrated that mechanical vibration can influence bed hydrodynamics even at comparatively low vibration intensities. Reported effects include reductions in minimum fluidization and minimum bubbling velocities [3,51], modifications of solids circulation patterns [23], changes in bed expansion behavior [51], and enhanced gas-solids mixing [22]. In several of these studies, the magnitude of the observed effects increased with vibration intensity. Moreover, a significant portion of the reported results corresponds to operating conditions in the vicinity of minimum fluidization, where gas-driven momentum is comparatively low and vibration-induced motion can contribute more strongly to particle dynamics. In contrast, the present study examines fully developed bubbling at superficial gas velocities well above the minimum fluidization velocity. Under these conditions, the combination of relatively low vibration intensity and operation in a gas-dominated regime causes bubble formation, growth, and rise to be primarily governed by gas-driven hydrodynamics. The additional motion induced by the applied vibration amplitude and frequency therefore remains small relative to gas-induced particle circulation and is further attenuated by inertial damping within the dense Geldart Group D particle bed. As a result, no pronounced qualitative changes in instantaneous bubble morphology or rise behavior are observed for the investigated vibration conditions.

The following sections build on these qualitative observations by providing a quantitative comparison of bed height, bubble diameter, bubble count, and bubble rise velocity, with particular emphasis on the differences between slice-based and full three-dimensional analyses.

4.2. Bed height

The bed heights for the MRI measurements, the three-dimensional CFD-DEM data, and the central slice extracted from the simulations were determined as described in Section 2.2. Fig. 4 shows the time-averaged bed heights for vibration frequencies of 0, 10, 20, and 30 Hz at superficial gas velocities of $U_{f,in} = 2$, 3, and 4 U_{mf}. The reported mean values represent averages over the full 9 s sampling duration and three independent repetitions. The observed trends were consistent across repetitions, and no systematic temporal drift was detected within the recorded time window.

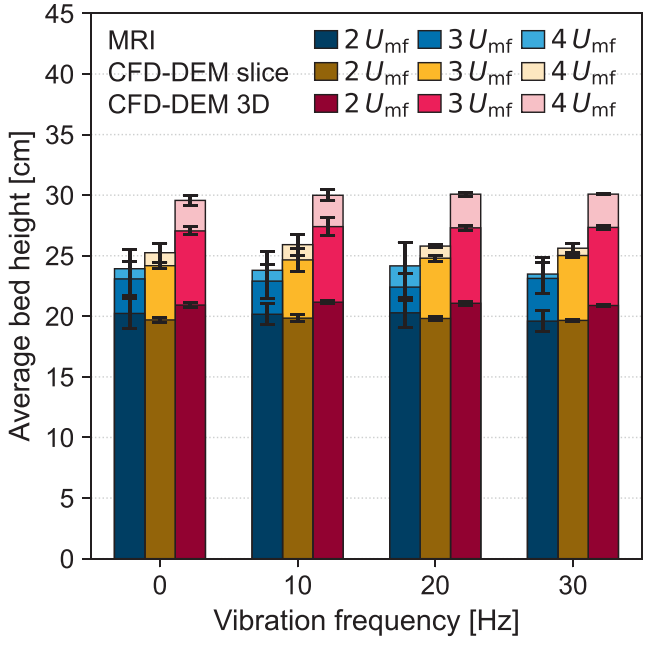

Fig. 4. Comparison of experimentally measured and simulated (slice and 3D method) averaged bed height at a flow of $U_{f,in} = 2\ U_{mf}$, $U_{f,in} = 3\ U_{mf}$, and $U_{f,in} = 4\ U_{mf}$ and vibration frequencies of 0 Hz, 10 Hz, 20 Hz, and 30 Hz.

For the non-vibrated case, the average bed height increases with increasing superficial gas velocity, as expected for bubbling fluidization due to increased gas holdup and bubble volume fraction. The CFD-DEM slice results show very close agreement with the MRI measurements at 2 U_{mf}. At 3 and 4 U_{mf}, the slice-based simulation results are moderately higher than the MRI data, with an average deviation of approximately 7.7%. Despite this deviation, the slice-based approach reproduces the velocity-dependent increase in bed height consistently. By comparison, the bed heights obtained from the full three-dimensional CFD-DEM data are consistently higher than both the MRI and slice-based results, with the deviation becoming more pronounced at 3 and 4 U_{mf}. This systematic difference between slice-based and full three-dimensional evaluation arises from the bed-height definition. In the three-dimensional data, the highest particle-containing point across the entire bed cross-section is considered, whereas the MRI and CFD-DEM slice-based methods only capture fluctuations within the central 10 mm region. Because bubble eruptions and local surface fluctuations occur throughout the bed cross-section, the absolute maximum bed height is not necessarily located within the central slice. As a result, slice-based measurements systematically underestimate the global bed expansion compared to full three-dimensional evaluation.

When comparing vibrated and non-vibrated cases, no systematic change in average bed height beyond experimental and numerical uncertainties is observed for the investigated frequencies and gas velocities. The trends established for the non-vibrated case are preserved: slice-based CFD-DEM results remain in close agreement with MRI measurements, while full three-dimensional results consistently yield higher absolute bed heights. The limited influence of vibration on average bed height can be interpreted in light of the operating regime discussed in Section 4.1. Under the investigated conditions, the time-averaged bed expansion is governed by gas-driven bubble formation and eruption. While vibration introduces an additional oscillatory acceleration, no measurable change in the mean bed height is observed. This indicates that any direct displacement induced by vibration, as well as any potential vibration-induced modification of bubbling behavior, remain small relative to the gas-driven contribution to bed expansion within the investigated parameter range.

4.3. Bubble diameter

Fig. 5 compares the bubble diameters measured from MRI data, CFD-DEM simulations (slice and 3D analysis), and established correlations from Kato & Wen [52], Werther [53], and Darton et al. [54] as a function of distance from the distributor for superficial gas velocities of $U_{f,in} = 2$, 3, and 4 U_{mf}.

At lower bed heights, good agreement is observed between all methods and the established correlations, indicating that initial bubble growth is reasonably described by classical scaling relationships. However, at greater heights and at gas velocities of 3 and 4 U_{mf}, both experimental and numerical results deviate from the approximately linear bubble growth predicted by the correlations. Instead, bubble growth is reduced, and in some cases, a decrease in bubble diameter is observed. Several mechanisms contribute to this behavior. First, large bubbles approaching the surface erupt, limiting further vertical growth, while smaller bubbles are still able to exist without being in contact with the surface. Second, bubble growth is constrained by the finite bed diameter of 96 mm. At higher bed heights, the average bubble diameters reach approximately 0.5–0.7 times the bed diameter, indicating significant lateral confinement. Individual bubbles occasionally exhibit area-equivalent diameters exceeding the bed diameter due to their elongated shapes. Under such conditions, bubble coalescence and expansion are increasingly restricted by wall effects, and the system approaches the onset of slugging behavior. These confinement effects are not accounted for in the classical correlations, which are primarily derived for larger or effectively unconfined beds, and therefore tend to overpredict bubble growth in the present geometry.

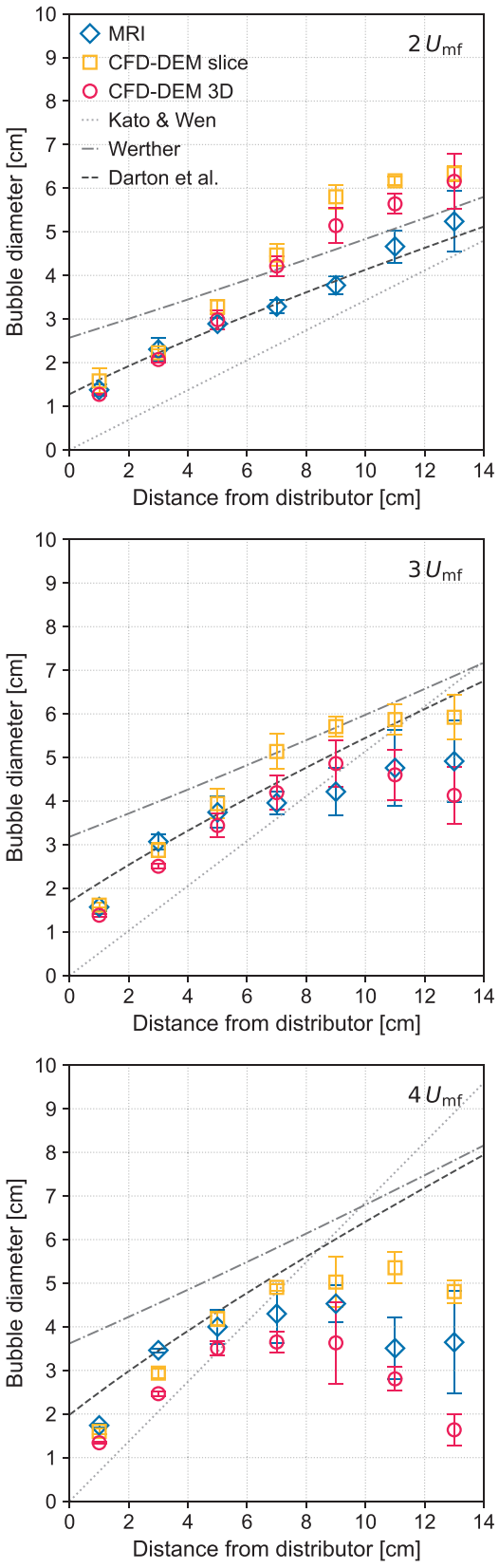

Fig. 5. Comparison of experimentally measured, simulated (slice and 3D method) bubble diameter, and correlations for bubble diameter by Kato & Wen [52], Werther [53], and Darton et al. [54] as a function of distance from the distributor. From top to bottom diagrams show flow of $U_{f,in} = 2$ U_{mf}, $U_{f,in} = 3$ U_{mf}, and $U_{f,in} = 4$ U_{mf}.

Regarding the comparison between analysis methods, the CFD-DEM slice method tends to overpredict bubble diameters relative to MRI measurements at higher bed heights, while the full three-dimensional analysis consistently yields lower values than the slice-based analysis. This difference arises from sampling effects: the slice method primarily captures centrally located, larger bubbles, whereas the three-dimensional evaluation includes smaller off-center bubbles that are not always intersected by the central slice. As not all bubbles coalesce during their ascent and bubble splitting events generate additional smaller bubbles, their inclusion in the three-dimensional analysis lowers the overall average diameter.

Fig. 6 presents the corresponding bubble diameter data for vibration frequencies of 10, 20, and 30 Hz (0.5 mm peak-to-peak amplitude). Within the investigated vibration intensity range ($\Gamma < 1$), no systematic change in bubble growth behavior is observed compared to the non-vibrated cases. The same confinement-induced deviation from classical correlations and the same methodological differences between slice-based and three-dimensional analyses persist across all vibration frequencies. This indicates that, under the present gas-dominated bubbling conditions, vibration does not substantially modify the bubble growth characteristics.

4.4. Number of bubbles

Fig. 7 compares the number of bubbles per frame as a function of distance from the distributor for the MRI measurements and CFD-DEM

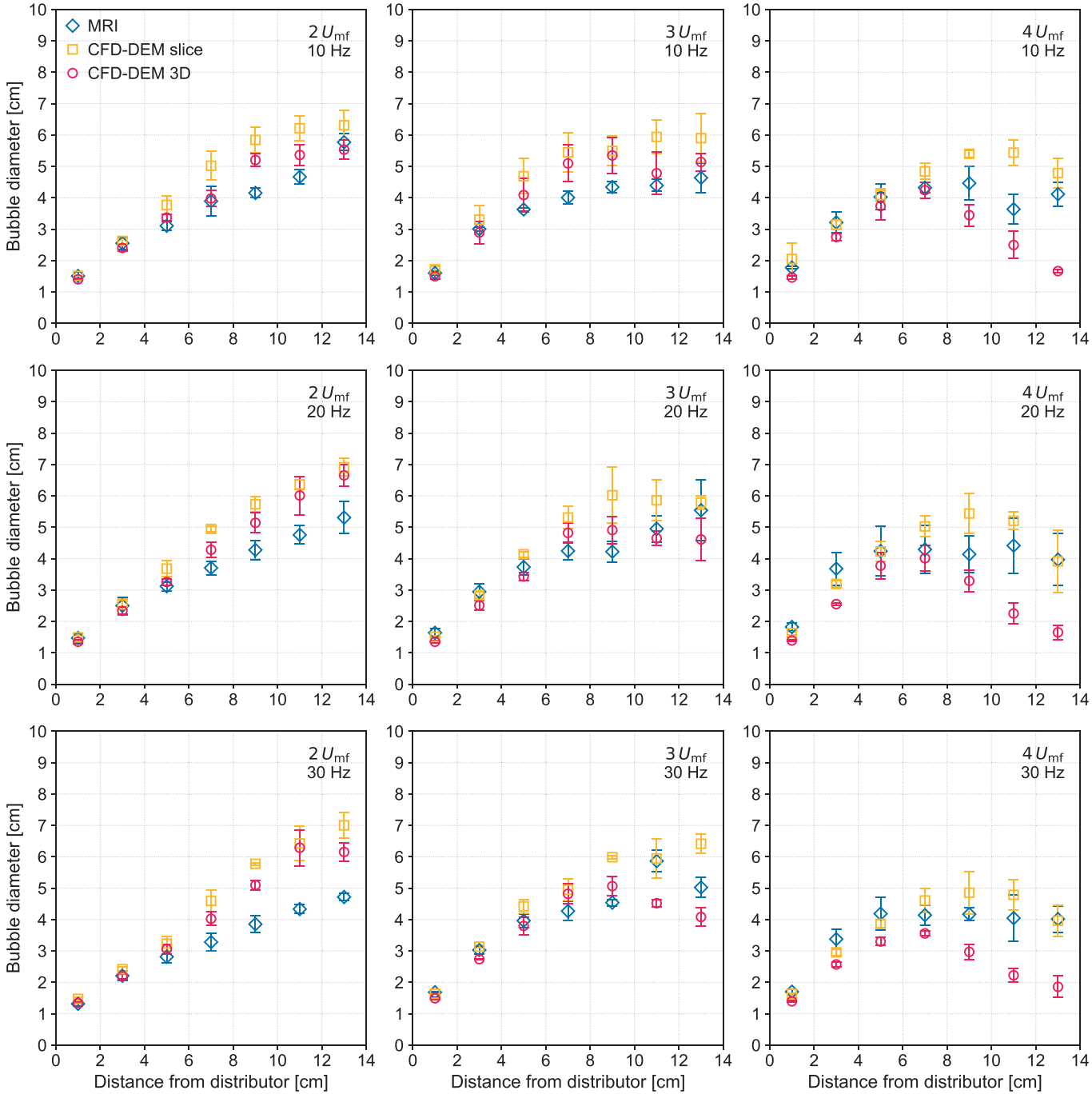

Fig. 6. Comparison of experimentally measured and simulated (slice and 3D method) bubble diameter as a function of distance from the distributor. From left to right columns show flow of $U_{f,in} = 2\ U_{mf}$, $U_{f,in} = 3\ U_{mf}$, and $U_{f,in} = 4\ U_{mf}$ and rows top to bottom give vibration frequencies of 10 Hz, 20 Hz, and 30 Hz.

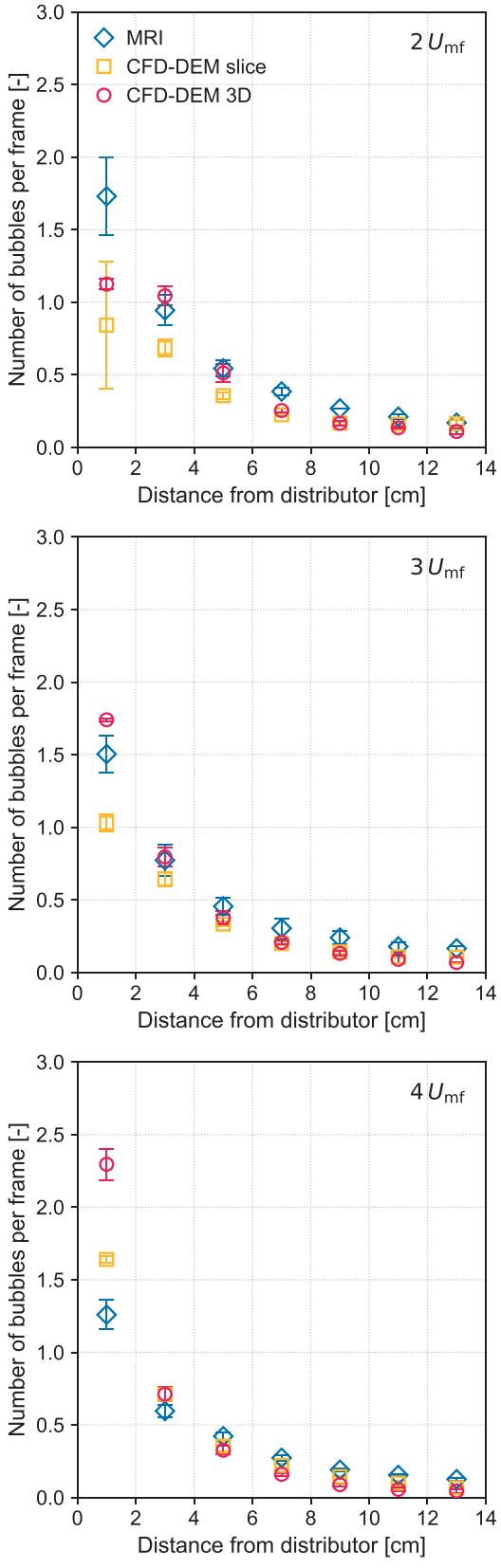

Fig. 7. Comparison of experimentally measured and simulated (slice and 3D method) number of bubbles per frame as a function of distance from the distributor. From top to bottom diagrams show flow of $U_{f,in} = 2\ U_{mf}$, $U_{f,in} = 3\ U_{mf}$, and $U_{f,in} = 4\ U_{mf}$.

simulations (slice and 3D method) at superficial gas velocities of $U_{f,in} =$ 2, 3, and 4 U_{mf}.

All methods show a consistent decrease in bubble count with increasing bed height, reflecting progressive bubble coalescence during ascent. This trend agrees with previous observations for bubbling beds of Geldart Group D particles [16]. The highest bubble numbers occur near the distributor, where bubble nucleation dominates. At low bed heights, the CFD-DEM simulations show an increase in bubble count with increasing superficial gas velocity, consistent with enhanced gas throughput and nucleation frequency. The MRI measurements do not exhibit this trend. Several factors may contribute to this discrepancy. First, the spatial resolution and threshold-based segmentation of the MRI data limit the reliable detection of very small bubbles near the distributor, particularly under more dilute conditions at higher gas velocities, where gas-solid interfaces become less sharply defined. Second, the numerical representation of the distributor as a uniform velocity inlet neglects possible local non-uniformities in gas injection that may influence initial bubble formation. In experimental systems, small-scale maldistribution or preferential gas pathways can affect the number and size of incipient bubbles. Third, the assumption of spherical particles in the DEM model, despite a measured sphericity of 0.87, may influence local packing structure, contact mechanics, and gas percolation pathways in the dense region close to the distributor. Although the DEM parameters are calibrated to reproduce bulk properties such as angle of repose, bulk friction, cohesion, and density, this calibration ensures agreement primarily at the macroscopic level. Local microstructural arrangements near the distributor may still differ between real and modeled particles, potentially affecting bubble initiation and stability. Overall, these considerations indicate that discrepancies near the distributor likely result from the combined influence of measurement limitations and modeling assumptions. In contrast to the findings of Penn et al. [16], who reported an increase in bubble count with increasing superficial gas velocity at higher vertical positions in a 190 mm diameter bed, neither the MRI measurements nor the CFD-DEM simulations in the present study show a comparable trend. This difference is likely related to the smaller bed diameter (96 mm) used here, which enhances lateral confinement and promotes earlier coalescence, particularly at higher gas velocities, where bubble diameters approach a significant fraction of the bed diameter. The resulting proximity to slugging conditions limits the persistence of multiple discrete bubbles at higher positions in the bed.

At greater bed heights, bubble counts from all methods converge toward similarly low values due to extensive coalescence. In this region, methodological differences between slice-based and three-dimensional analyses become less pronounced because large, centrally located bubbles dominate the bed cross-section. At lower bed heights, clearer differences between analysis methods are observed. Consistent with the bubble diameter results, the full three-dimensional analysis yields higher bubble counts than the slice-based method, as it captures smaller off-center bubbles that are not always intersected by the central slice. Conversely, the slice-based method may underrepresent the total bubble population due to its limited spatial sampling.

Fig. 8 shows the number of bubbles per frame for vibration frequencies of 10, 20, and 30 Hz (0.5 mm peak-to-peak amplitude). Across all frequencies, the overall bubble count distributions closely resemble the non-vibrated results. The height-dependent decrease due to coalescence and the differences between slice-based and three-dimensional analyses persist under vibrated conditions, indicating that vibration does not measurably alter bubble nucleation or coalescence dynamics within the investigated parameter range.

4.5. *Bubble rise velocity*

Fig. 9 compares the bubble rise velocities obtained from MRI measurements, CFD-DEM simulations (slice and 3D analysis), and established correlations from Hilligardt & Werther [55], Werther [53], and

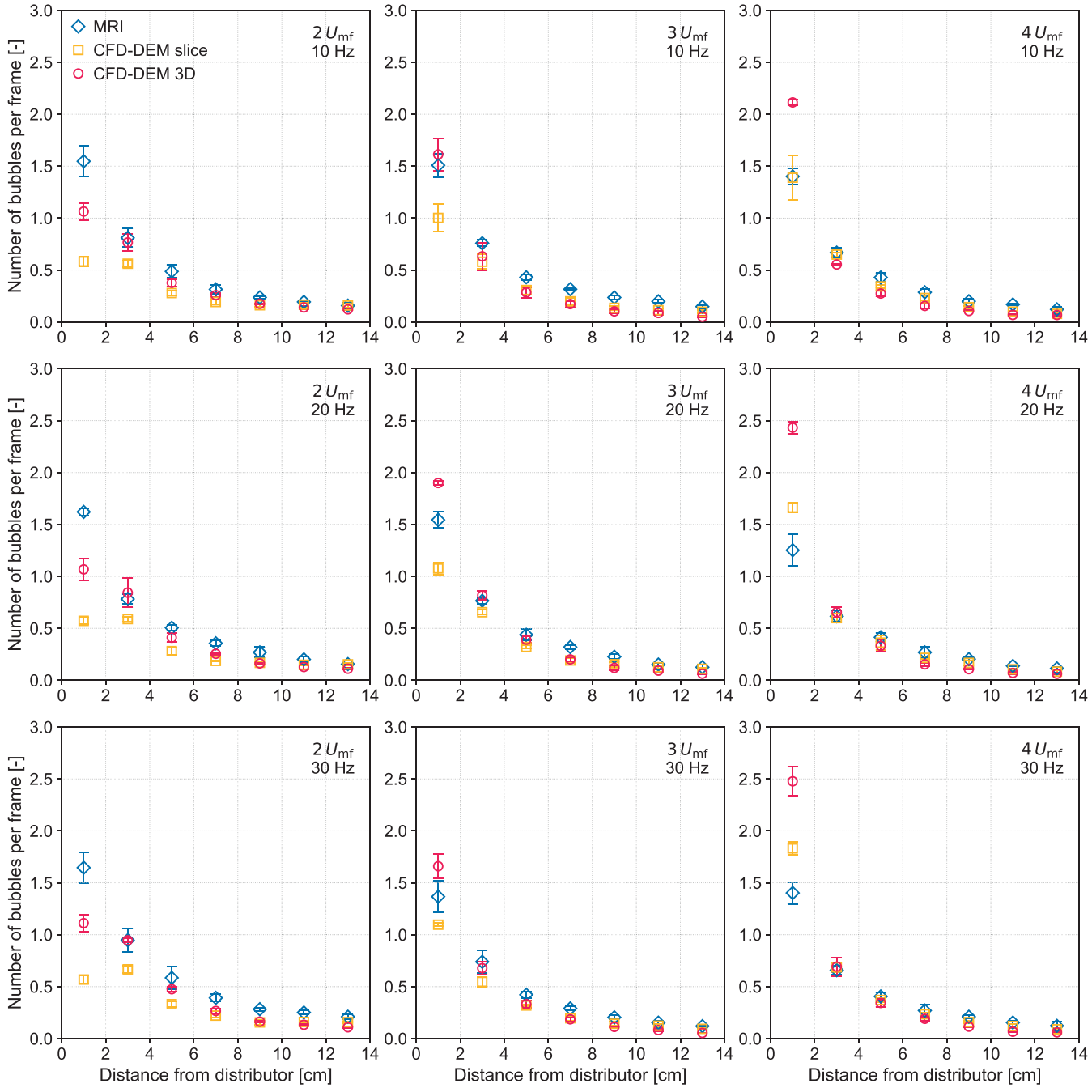

Fig. 8. Comparison of experimentally measured and simulated (slice and 3D method) number of bubbles as a function of distance from the distributor. From left to right columns show flow of $U_{f,in} = 2\ U_{mf}$, $U_{f,in} = 3\ U_{mf}$, and $U_{f,in} = 4\ U_{mf}$ and rows top to bottom give vibration frequencies of 10 Hz, 20 Hz, and 30 Hz.

Donsi et al. [56] as a function of bubble diameter for superficial gas velocities of $U_{f,in} = 2$, 3, and 4 U_{mf}.

All methods show the expected increase in rise velocity with increasing bubble diameter, consistent with buoyancy-driven bubble motion in bubbling fluidized beds. At 2 U_{mf}, good agreement is observed between measurements, simulations, and correlations across the full bubble diameter range, although the Donsi et al. [56] correlation predicts slightly lower bubble rise velocities for larger diameters. Since the Werther [53] and Donsi et al. [56] correlations do not include superficial gas velocity explicitly, they predict identical bubble rise velocities for 2, 3, and 4 U_{mf}. In contrast, the Hilligardt & Werther [55] correlation accounts for superficial gas velocity and therefore predicts increasing bubble rise velocities with increasing gas throughput. For smaller bubble diameters, the MRI measurements and both CFD-DEM methods show only minor dependence of rise velocity on superficial gas velocity, indicating that small-bubble motion is primarily governed by local buoyancy and surrounding solids dynamics rather than bulk gas throughput. For larger diameters, a clearer velocity dependence is observed. The MRI data show an increase in bubble rise velocity from 2 to 3 U_{mf}, followed by a slight reduction at 4 U_{mf}. However, the significance of this trend is uncertain due to the larger standard deviations at elevated gas velocities and the reduced number of large bubbles contributing to the averages. The CFD-DEM simulations, particularly the slice-based method, exhibit a more pronounced increase in bubble rise velocity with increasing gas velocity for larger diameters, in closer agreement with the Hilligardt & Werther [55] correlation.

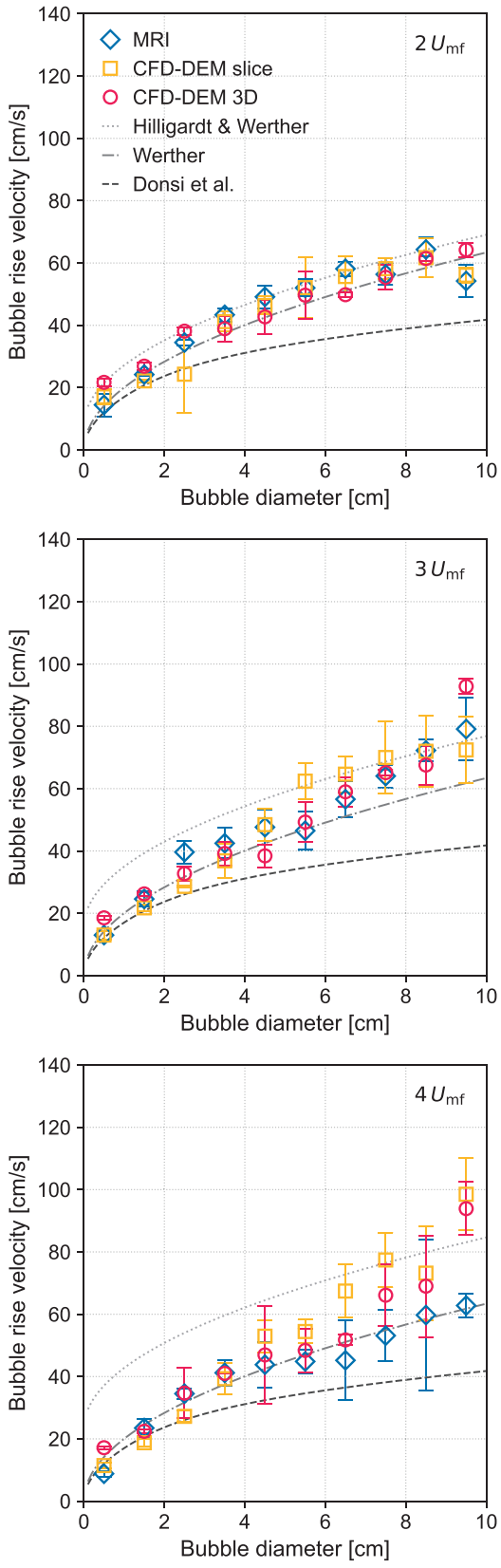

Fig. 9. Comparison of experimentally measured, simulated (slice and 3D method) bubble rise velocity, and correlations for bubble rise velocity by Hilligardt & Werther [55], Werther [53], and Donsi et al. [56] as a function of bubble diameter. From top to bottom diagrams show flow of $U_{f,in} = 2\ U_{mf}$, $U_{f,in} = 3\ U_{mf}$, and $U_{f,in} = 4\ U_{mf}$.

Fig. 10 presents the corresponding results for vibration frequencies of 10, 20, and 30 Hz (0.5 mm peak-to-peak amplitude). Across all frequencies, the relationship between bubble diameter and rise velocity remains consistent with the non-vibrated results. The dependence of rise velocity on bubble size and gas velocity is preserved, and the quantitative agreement between MRI and CFD-DEM simulations remains unchanged. These findings indicate that, within the investigated parameter range, vibration does not measurably modify the buoyancy-driven rise dynamics of bubbles in the fully developed bubbling regime.

4.6. *Interpretation of vibration effects and methodological implications*

The quantitative results presented in Sections 4.2–4.5 allow a consolidated interpretation of the role of vibration under the investigated operating conditions for Geldart Group D particles. Across all examined quantities, including bed height, bubble diameter, bubble count, and bubble rise velocity, no systematic modification of bubbling behavior was observed for vibration intensities $\Gamma < 1$ at superficial gas velocities of 2–4 Umf. Sections 4.3–4.5 demonstrate that vibration does not measurably alter bubble growth, coalescence behavior, bubble population density, or the relationship between bubble diameter and rise velocity. Since time-averaged bed height in the bubbling regime is governed by the spatial distribution and dynamics of gas bubbles, the absence of significant changes at the bubble scale directly explains the unchanged average bed heights reported in Section 4.2. The bed-height results are therefore consistent with, and supported by, the bubble-scale analysis rather than representing an independent observation. These findings indicate that, for Geldart Group D particles operating well above minimum fluidization and at $\Gamma < 1$, bed hydrodynamics are governed primarily by gas-driven bubbling, with vibration acting only as a secondary perturbation that does not introduce measurable changes to the macroscopic flow behavior.

In addition, the comparison between slice-based and full three-dimensional analyses provides insight into measurement representativeness. While slice-based evaluation reproduces the main hydrodynamic trends observed experimentally, the full three-dimensional analysis reveals systematic differences in absolute values, particularly for bed height and small-bubble statistics. These findings indicate that central-slice measurements are suitable for capturing trend behavior but may underestimate global extrema or off-center bubble populations in cylindrical beds. This has implications beyond the present study. Many MRI and related tomographic investigations rely on limited spatial sampling. The present results highlight the importance of considering sampling geometry when interpreting absolute hydrodynamic quantities. The combined use of MRI and three-dimensional CFD-DEM therefore provides complementary insight and strengthens confidence in the interpretation of hydrodynamic behavior.

5. Conclusion

This study investigated the hydrodynamics and gas bubble properties of non-vibrated and vibrated fluidized beds of small Geldart Group D particles using real-time MRI measurements and CFD-DEM simulations. The investigation covered superficial gas velocities of $U_{f,in} = 2$, 3, and 4 U_{mf} with vibration frequencies of 10, 20, and 30 Hz at a peak-to-peak amplitude of 0.5 mm. Two different analysis methods were employed for the simulation data: evaluation of the central 10 mm slice of the fluidized bed to directly mimic the MRI measurement approach and enable accurate comparison, and evaluation of the entire three-dimensional simulation domain to assess whether slice-based results are transferable to the full three-dimensional system.

For the non-vibrated fluidized beds, MRI measurements and CFD-DEM simulations showed strong agreement across bubble behavior and all investigated hydrodynamic properties. The CFD-DEM slice method successfully reproduced the trends observed in MRI measurements for bed height, bubble diameter evolution with height, bubble

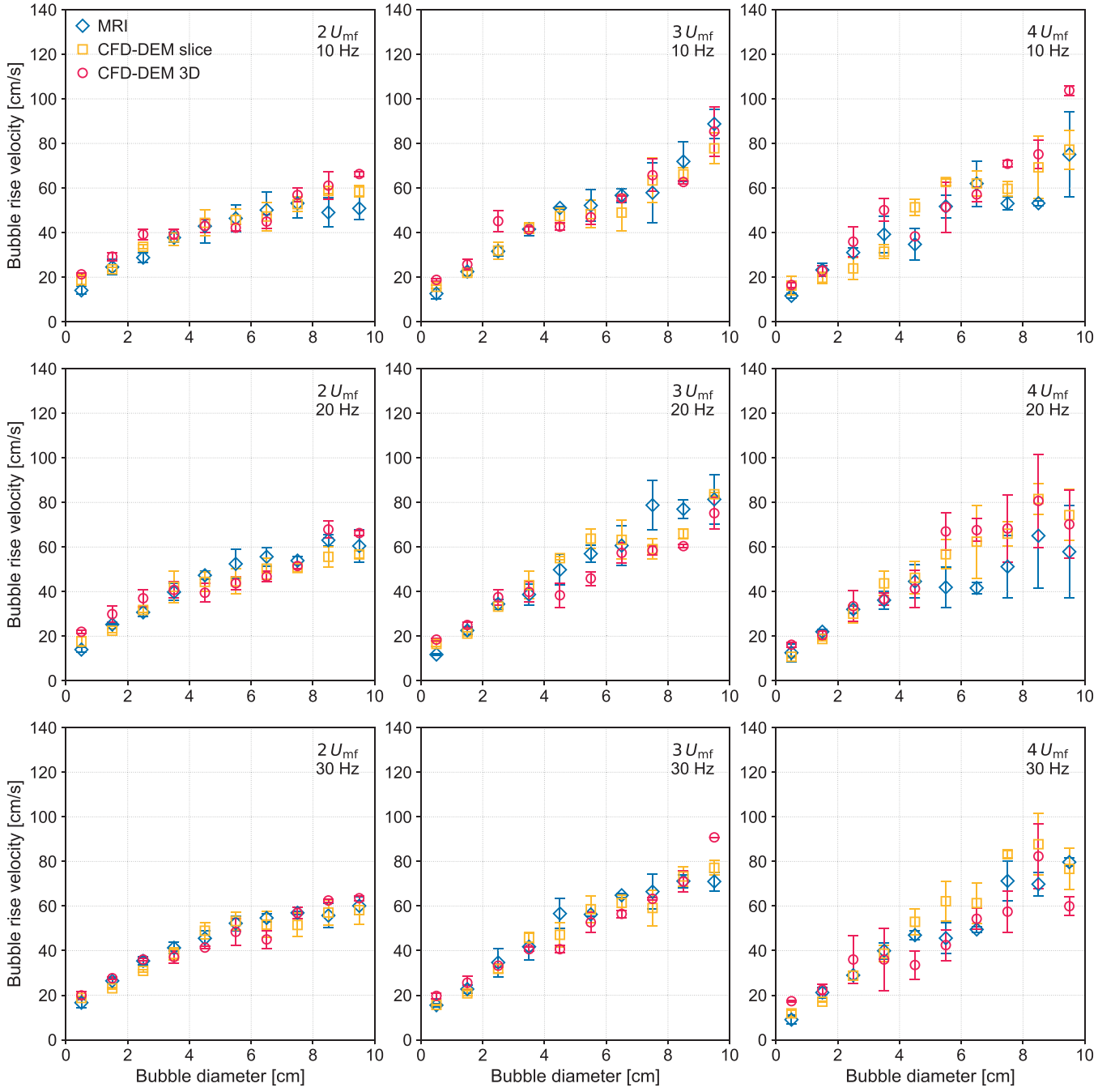

Fig. 10. Comparison of experimentally measured and simulated (slice and 3D method) bubble rise velocity as a function of bubble diameter. From left to right columns show flow of $U_{f,in} = 2\ U_{mf}$, $U_{f,in} = 3\ U_{mf}$, and $U_{f,in} = 4\ U_{mf}$ and rows top to bottom give vibration frequencies of 10 Hz, 20 Hz, and 30 Hz.

count distribution over height, and bubble rise velocity as a function of bubble diameter across all tested superficial gas velocities. Nonetheless, some small but systematic deviations were observed: at lower superficial gas velocities, bubble diameters at higher bed heights were slightly overpredicted and the number of bubbles near the distributor was underpredicted, while at higher gas velocities, bed heights were moderately overestimated compared to MRI data. Both experimental and simulation results also showed good agreement with established correlations for bubble diameter (Kato & Wen [52], Werther [53], and Darton et al. [54]) and with bubble rise velocity correlations (Hilligardt & Werther [55], Werther [53], and Donsi et al. [56]) across the investigated operating range.

For vibrated conditions, no systematic modification of bubbling behavior was observed for $\Gamma < 1$ within the investigated gas velocity range. These results indicate that, for Geldart Group D particles operating well above minimum fluidization, low-to-moderate vibration intensities do not substantially alter macroscopic bubbling characteristics. The influence of vibration is therefore likely confined to operating regimes closer to minimum fluidization, higher vibration intensities, or particle systems with different material properties.

The full three-dimensional analysis of the simulation data revealed systematic differences in absolute quantities compared to the slice-based analysis. The three-dimensional analysis consistently showed higher bed heights, particularly at elevated gas velocities, due to its ability to capture bubble eruptions and surface fluctuations occurring across the entire bed cross-section rather than only in the central region. For

bubble diameter analysis, the three-dimensional method generally yielded lower average values than the slice method at higher bed heights, as it detected smaller bubbles distributed throughout the bed that were not intersected by the central slice. Conversely, for bubble count, the three-dimensional method consistently detected more bubbles, especially near the distributor. These systematic differences demonstrate that while central-slice analysis captures overall hydrodynamic trends, it may not fully represent global three-dimensional quantities, particularly bed height and small-bubble statistics. This highlights the importance of considering spatial sampling limitations when interpreting tomographic measurements.

The present validation focuses primarily on bubble-scale observables, namely bed height, bubble diameter, bubble count, and bubble rise velocity, which represent central descriptors of bubbling hydrodynamics and are directly accessible from real-time MRI measurements. These quantities capture key aspects of macroscopic bed behavior; however, relying exclusively on bubble-scale metrics does not fully assess all features of gas-solid interaction dynamics. The good agreement at the bubble scale supports the CFD-DEM model's ability to reproduce dominant hydrodynamic structures, yet additional validation at the level of pressure dynamics and solids kinematics would further strengthen confidence in its general predictive capability. Future work should therefore extend model assessment to such additional hydrodynamic metrics and explore a broader range of vibration intensities, particle classes, and bed geometries to further delineate the parameter space in which vibration effects become significant.

CRediT authorship contribution statement

Nick Hildebrandt: Writing – review & editing, Writing – original draft, Visualization, Validation, Software, Methodology, Investigation, Formal analysis, Data curation, Conceptualization. **Melis Özdemir:** Writing – review & editing, Writing – original draft, Visualization, Validation, Software, Methodology, Investigation, Formal analysis, Data curation, Conceptualization. **Swantje Pietsch-Braune:** Writing – review & editing, Supervision, Project administration, Conceptualization. **Stefan Benders:** Writing – review & editing, Supervision, Project administration, Conceptualization. **Alexander Penn:** Writing – review & editing, Supervision, Resources, Project administration, Funding acquisition, Conceptualization. **Stefan Heinrich:** Writing – review & editing, Supervision, Resources, Project administration, Funding acquisition, Conceptualization.

Declaration of generative AI and AI-assisted technologies in the writing process

During the preparation of this work, the authors used Claude Sonnet 4 and ChatGPT-5.2 to rearrange and reword sentences for improved readability. After using this tool, the authors reviewed and edited the content as needed and take full responsibility for the content of the published article.

Declaration of competing interest

The authors declare that they have no known competing financial interests or personal relationships that could have appeared to influence the work reported in this paper.

Acknowledgments

This work was funded by the German Research Foundation (DFG) under project number 471615686. Moreover, the authors gratefully acknowledge partial funding of this project by German Research Foundation (DFG) under SFB 1615–503850735.

Appendix A. Supplementary data

Supplementary data to this article can be found online at https://doi.org/10.1016/j.powtec.2026.122468.

Data availability

Data will be made available on request.

References

[1] E. Marring, A.C. Hoffmann, L.P.B.M. Janssen, The effect of vibration on the fluidization behaviour of some cohesive powders, Powder Technol. 79 (1994) 1–10, https://doi.org/10.1016/0032-5910(94)02810-9.
[2] Y. Mawatari, Y. Tatemoto, K. Noda, Prediction of minimum fluidization velocity for vibrated fluidized bed, Powder Technol. 131 (2003) 66–70, https://doi.org/10.1016/S0032-5910(02)00323-6.
[3] C.P. McLaren, J.P. Metzger, C.M. Boyce, C.R. Müller, Reduction in minimum fluidization velocity and minimum bubbling velocity in gas-solid fluidized beds due to vibration, Powder Technol. 382 (2021) 566–572, https://doi.org/10.1016/j.powtec.2021.01.023.
[4] S.E. Lehmann, E.-U. Hartge, A. Jongsma, I.-M. deLeeuw, F. Innings, S. Heinrich, Fluidization characteristics of cohesive powders in vibrated fluidized bed drying at low vibration frequencies, Powder Technol. 357 (2019) 54–63, https://doi.org/10.1016/j.powtec.2019.08.105.
[5] H. Jin, Z. Tong, J. Zhang, B. Zhang, Homogeneous fluidization characteristics of vibrating fluidized beds, Can. J. Chem. Eng. 82 (2004) 1048–1053, https://doi.org/10.1002/cjce.5450820521.
[6] D. Barletta, M. Poletto, Aggregation phenomena in fluidization of cohesive powders assisted by mechanical vibrations, Powder Technol. 225 (2012) 93–100, https://doi.org/10.1016/j.powtec.2012.03.038.
[7] Y. Mawatari, M. Tsunekawa, Y. Tatemoto, K. Noda, Favorable vibrated fluidization conditions for cohesive fine particles, Powder Technol. 154 (2005) 54–60, https://doi.org/10.1016/j.powtec.2005.04.026.
[8] F. Hernández-Jiménez, J. Sánchez-Prieto, A. Soria-Verdugo, A. Acosta-Iborra, Experimental quantification of the particle–wall frictional forces in pseudo-2D gas fluidised beds, Chem. Eng. Sci. 102 (2013) 257–267, https://doi.org/10.1016/j.ces.2013.08.020.
[9] T. Li, P. Gopalakrishnan, R. Garg, M. Shahnam, CFD–DEM study of effect of bed thickness for bubbling fluidized beds, Particuology 10 (2012) 532–541, https://doi.org/10.1016/j.partic.2012.02.006.
[10] R.F. Mudde, Time-resolved X-ray tomography of a fluidized bed, Powder Technol. 199 (2010) 55–59, https://doi.org/10.1016/j.powtec.2009.04.021.
[11] F. Wang, Q. Marashdeh, L.-S. Fan, W. Warsito, Electrical capacitance volume tomography: design and applications, Sensors 10 (2010) 1890–1917, https://doi.org/10.3390/s100301890.
[12] B. Watson, L. Lindmüller, S. Heinrich, J. Theuerkauf, Y. Yao, Y. Fan, Dynamic bubble tracking in fluidized beds via electrical capacitance volume tomography, Chem. Eng. J. 487 (2024) 150461, https://doi.org/10.1016/j.cej.2024.150461.
[13] M. Stein, Y.L. Ding, J.P.K. Seville, D.J. Parker, Solids motion in bubbling gas fluidised beds, Chem. Eng. Sci. 55 (2000) 5291–5300, https://doi.org/10.1016/S0009-2509(00)00177-9.
[14] C.R. Müller, D.J. Holland, A.J. Sederman, M.D. Mantle, L.F. Gladden, J. F. Davidson, Magnetic resonance imaging of fluidized beds, Powder Technol. 183 (2008) 53–62, https://doi.org/10.1016/j.powtec.2007.11.029.
[15] A. Penn, T. Tsuji, D.O. Brunner, C.M. Boyce, K.P. Pruessmann, C.R. Müller, Real-time probing of granular dynamics with magnetic resonance, Sci. Adv. 3 (2017) e1701879, https://doi.org/10.1126/sciadv.1701879.
[16] A. Penn, C.M. Boyce, T. Kovar, T. Tsuji, K.P. Pruessmann, C.R. Müller, Real-time magnetic resonance imaging of bubble behavior and particle velocity in fluidized beds, Ind. Eng. Chem. Res. 57 (2018) 9674–9682, https://doi.org/10.1021/acs.iecr.8b00932.
[17] C.M. Boyce, A. Penn, K.P. Pruessmann, C.R. Müller, Magnetic resonance imaging of gas–solid fluidization with liquid bridging, AICHE J. 64 (2018) 2958–2971, https://doi.org/10.1002/aic.16036.
[18] C.M. Boyce, A. Penn, M. Lehnert, K.P. Pruessmann, C.R. Müller, Magnetic resonance imaging of single bubbles injected into incipiently fluidized beds, Chem. Eng. Sci. 200 (2019) 147–166, https://doi.org/10.1016/j.ces.2019.01.047.
[19] A. Penn, C.M. Boyce, N. Conzelmann, G. Bezinge, K.P. Pruessmann, C.R. Müller, Real-time magnetic resonance imaging of fluidized beds with internals, Chem. Eng. Sci. 198 (2019) 117–123, https://doi.org/10.1016/j.ces.2018.12.041.
[20] H.S. Rennebaum, D.L. Brummerloh, S. Benders, A. Penn, The effect of baffles on the hydrodynamics of a gas-solid fluidized bed studied using real-time magnetic resonance imaging, Powder Technol. 432 (2024) 119114, https://doi.org/10.1016/j.powtec.2023.119114.
[21] H.S. Rennebaum, C.R. Müller, A. Penn, Vertical tubes in bubbling fluidized beds: a magnetic resonance imaging study of particle and bubble behavior, Powder Technol. 457 (2025) 120870, https://doi.org/10.1016/j.powtec.2025.120870.
[22] M.J.A. De Munck, E.A.J.F. Peters, J.A.M. Kuipers, Experimental study on vibrating fluidized bed solids drying, Chem. Eng. J. 472 (2023) 144809, https://doi.org/10.1016/j.cej.2023.144809.

[23] C. Zeilstra, M.A. Van Der Hoef, J.A.M. Kuipers, Experimental and numerical study of solids circulation in gas-vibro fluidized beds, Powder Technol. 248 (2013) 153–160, https://doi.org/10.1016/j.powtec.2013.03.045.
[24] Y. Zhang, J. Zhang, Y. Zhao, X. Zhang, X. Yang, E. Zhou, C. Duan, G. Wang, L. Dong, Investigations on dynamics of bubble in a 2D vibrated fluidized bed using pressure drop signal and high-speed image analysis, Chem. Eng. J. 395 (2020) 125129, https://doi.org/10.1016/j.cej.2020.125129.
[25] E. Cano-Pleite, F. Hernández-Jiménez, M. De Vega, A. Acosta-Iborra, Experimental study on the motion of isolated bubbles in a vertically vibrated fluidized bed, Chem. Eng. J. 255 (2014) 114–125, https://doi.org/10.1016/j.cej.2014.06.016.
[26] Q. Guo, Y. Zhang, A. Padash, K. Xi, T.M. Kovar, C.M. Boyce, Dynamically structured bubbling in vibrated gas-fluidized granular materials, Proc. Natl. Acad. Sci. USA 118 (2021) e2108647118, https://doi.org/10.1073/pnas.2108647118.
[27] D. Liu, B. Van Wachem, Comprehensive assessment of the accuracy of CFD-DEM simulations of bubbling fluidized beds, Powder Technol. 343 (2019) 145–158, https://doi.org/10.1016/j.powtec.2018.11.025.
[28] K. Xi, T. Kovar, W.D. Fullmer, A. Penn, J. Musser, C.M. Boyce, CFD-DEM study of bubble properties in a cylindrical fluidized bed of Geldart group D particles and comparison with prior MRI data, Powder Technol. 389 (2021) 75–84, https://doi.org/10.1016/j.powtec.2021.04.075.
[29] F. Alobaid, B. Epple, Improvement, validation and application of CFD/DEM model to dense gas–solid flow in a fluidized bed, Particuology 11 (2013) 514–526, https://doi.org/10.1016/j.partic.2012.05.008.
[30] C.P. McLaren, T.M. Kovar, A. Penn, C.R. Müller, C.M. Boyce, Gravitational instabilities in binary granular materials, Proc. Natl. Acad. Sci. USA 116 (2019) 9263–9268, https://doi.org/10.1073/pnas.1820820116.
[31] Z. Jiang, K. Rai, T. Tsuji, K. Washino, T. Tanaka, J. Oshitani, Upscaled DEM-CFD model for vibrated fluidized bed based on particle-scale similarities, Adv. Powder Technol. 31 (2020) 4598–4618, https://doi.org/10.1016/j.apt.2020.10.009.
[32] Q. Guo, C.M. Boyce, Structured bubbling in layered gas-fluidized beds subject to vibration: a CFD-DEM study, AICHE J. 68 (2022) e17709, https://doi.org/10.1002/aic.17709.
[33] Q. Guo, J. Tian, R. Huang, C.M. Boyce, Towards accurate modeling of vibration in CFD-DEM simulations of vibrated gas-fluidized beds without using a moving mesh, Chem. Eng. Sci. 298 (2024) 120445, https://doi.org/10.1016/j.ces.2024.120445.
[34] L. Xiang, W. Shuyan, L. Huilin, L. Goudong, C. Juhui, L. Yikun, Numerical simulation of particle motion in vibrated fluidized beds, Powder Technol. 197 (2010) 25–35, https://doi.org/10.1016/j.powtec.2009.08.016.
[35] Y. Tatemoto, Y. Mawatari, T. Yasukawa, K. Noda, Numerical simulation of particle motion in vibrated fluidized bed, Chem. Eng. Sci. 59 (2004) 437–447, https://doi.org/10.1016/j.ces.2003.10.005.
[36] K.P. Pruessmann, M. Weiger, M.B. Scheidegger, P. Boesiger, SENSE: sensitivity encoding for fast MRI, Magn. Reson. Med. 42 (1999) 952–962.
[37] H.G. Weller, G. Tabor, H. Jasak, C. Fureby, A tensorial approach to computational continuum mechanics using object-oriented techniques, Comput. Phys. 12 (1998) 620–631, https://doi.org/10.1063/1.168744.
[38] C. Kloss, C. Goniva, A. Hager, S. Amberger, S. Pirker, Models, algorithms and validation for opensource DEM and CFD-DEM, PCFD 12 (2012) 140, https://doi.org/10.1504/PCFD.2012.047457.
[39] C. Goniva, C. Kloss, N.G. Deen, J.A.M. Kuipers, S. Pirker, Influence of rolling friction on single spout fluidized bed simulation, Particuology 10 (2012) 582–591, https://doi.org/10.1016/j.partic.2012.05.002.
[40] J. Ding, D. Gidaspow, A bubbling fluidization model using kinetic theory of granular flow, AICHE J. 36 (1990) 523–538, https://doi.org/10.1002/aic.690360404.
[41] S. Ergun, Fluid flow through packed columns, Chem. Eng. Prog. 48 (1952) 89–94.
[42] C.Y. Wen, Y.H. Yu, Mechanics of fluidization, Chem. Eng. Prog. Symp. Ser. 62 (1966) 100–111.
[43] P.A. Cundall, O.D.L. Strack, A discrete numerical model for granular assemblies, Géotechnique 29 (1979) 47–65, https://doi.org/10.1680/geot.1979.29.1.47.
[44] Y. Tsuji, T. Tanaka, T. Ishida, Lagrangian numerical simulation of plug flow of cohesionless particles in a horizontal pipe, Powder Technol. 71 (1992) 239–250, https://doi.org/10.1016/0032-5910(92)88030-L.
[45] J. Ai, J.-F. Chen, J.M. Rotter, J.Y. Ooi, Assessment of rolling resistance models in discrete element simulations, Powder Technol. 206 (2011) 269–282, https://doi.org/10.1016/j.powtec.2010.09.030.
[46] H.P. Zhu, Z.Y. Zhou, R.Y. Yang, A.B. Yu, Discrete particle simulation of particulate systems: theoretical developments, Chem. Eng. Sci. 62 (2007) 3378–3396, https://doi.org/10.1016/j.ces.2006.12.089.
[47] Z. Peng, E. Doroodchi, C. Luo, B. Moghtaderi, Influence of void fraction calculation on fidelity of CFD-DEM simulation of gas-solid bubbling fluidized beds, AICHE J. 60 (2014) 2000–2018, https://doi.org/10.1002/aic.14421.
[48] C.M. Boyce, D.J. Holland, S.A. Scott, J.S. Dennis, Limitations on fluid grid sizing for using volume-averaged fluid equations in discrete element models of fluidized beds, Ind. Eng. Chem. Res. 54 (2015) 10684–10697, https://doi.org/10.1021/acs.iecr.5b03186.
[49] A. Acosta-Iborra, F. Hernández-Jiménez, M. De Vega, J.V. Briongos, A novel methodology for simulating vibrated fluidized beds using two-fluid models, Chem. Eng. J. 198–199 (2012) 261–274, https://doi.org/10.1016/j.cej.2012.05.098.
[50] Q. Guo, S. Chiu, W. Da, C.M. Boyce, Heat transfer within dynamically structured bubbling fluidized beds subject to vibration: a two-fluid modeling study, AICHE J. 69 (2023) e17970, https://doi.org/10.1002/aic.17970.
[51] X. Yang, Y. Zhang, Y. Yang, E. Zhou, Z. Fu, Y. Zhao, Fluidization of Geldart D type particles in a shallow vibrated gas-fluidized bed, Powder Technol. 305 (2017) 333–339, https://doi.org/10.1016/j.powtec.2016.09.044.
[52] K. Kato, C.Y. Wen, Bubble assemblage model for fluidized bed catalytic reactors, Chem. Eng. Sci. 24 (1969) 1351–1369, https://doi.org/10.1016/0009-2509(69)85055-4.
[53] J. Werther, Effect of gas distributor on the hydrodynamics of gas fluidized beds, German Chem. Eng. 1 (1978) 166–174.
[54] R.C. Darton, Bubble growth due to coalescence in fluidized beds, Trans. Inst. Chem. Eng. 55 (1977) 274–280.
[55] K. Hilligardt, J. Werther, Local bubble gas hold-up and expansion of gas/solid fluidized beds, German Chem. Eng. 9 (1986) 215–221.
[56] G. Donsì, L. Massimilla, S. Crescitelli, G. Volpicelli, Solid flow pattern at the wall of a fluidization column induced by single bubbles, Powder Technol. 6 (1972) 217–224, https://doi.org/10.1016/0032-5910(72)83015-8.